Comparison of nonlinear microscopy and frozen section histology for imaging of Mohs surgical margins

MICHAEL G. GIACOMELLI,[1] BEVERLY E. FAULKNER-JONES,[2] LUCAS C. CAHILL,[1] TADAYUKI YOSHITAKE,[1] DAIHUNG DO,[3] AND JAMES G. FUJIMOTO[1,*]

[1]*Massachusetts Institute of Technology, Department of Electrical Engineering and Computer Science and Research Laboratory of Electronics, 32 Vassar Street, Cambridge, MA 02139, USA*
[2]*Harvard Medical School, Department of Pathology, Beth Israel Deaconess Medical Center, 330 Brookline Avenue, Boston, MA 02215, USA*
[3]*Harvard Medical School, Department of Dermatology, Beth Israel Deaconess Medical Center, 330 Brookline Avenue, Boston, MA 02215, USA*
[*]jgfuji@mit.edu

Abstract: Mohs surgery uses *en face* frozen section analysis (FSA) with complete margin examination for the excision of select basal cell carcinomas (BCC), obtaining excellent cosmetic outcomes and extremely low recurrence rates. However, Mohs with FSA is time-consuming because of the need to iteratively perform cryosectioning on sequential excisions. Fluorescent microscopies can image tissue specimens without requiring physical sectioning, potentially reducing the time to perform Mohs surgery. We demonstrate a protocol for nonlinear microscopy (NLM) imaging of surgical specimens that combines dual agent staining, virtual H&E rendering, and video rate imaging. We also introduce a novel protocol that enables micron-level co-registration of NLM images with FSA histology, and demonstrate that NLM can reproduce similar features similar to FSA in BCC specimens with both negative and positive surgical margins. We show that the fluorescent labels can be extracted with conventional vacuum infiltration processing, enabling subsequent immunohistochemistry on fluorescently labeled tissue. This protocol can also be applied to evaluate the performance of NLM compared with FSA in a wide range of pathologies for intraoperative consultation.

1. Introduction

Keratinocytic carcinoma is the most common form of cancer in the US, with estimates as high as 5.4 million cases in 2012 [1], more than all other forms of cancer combined [2]. Furthermore, the incidence of keratinocytic carcinoma has increased 350% over the last 2 decades due to aging populations and increased sun exposure [1]. Mohs micrographic surgery uses intraoperative frozen section analysis (FSA) to assess margin status and is used in approximately one third of all Medicare reimbursed NMSC treatments [3]. Because the entire margin is evaluated, Mohs surgery has extremely low recurrence rates. A large study of BCC patients treated with Mohs found a 5 year recurrence rate of less than 2% [4].

In most Mohs procedures, although the excision is relatively rapid, the time required for FSA including freezing, cryosectioning and staining introduces substantial delay. As a result, the surgical time experienced by each patient can be very long because the surgeon operates on multiple patients, while patients wait for FSA histology to be available between excisions [5]. If specimens could be rapidly prepared and imaged, the surgeon could operate on one patient at a time, dramatically reducing each patient's surgical time. This would reduce patient anxiety and the amount of analgesic required, while simplifying clinic workflows. Therefore,

new technologies that enable rapid evaluation of specimens would reduce labor and processing delay as well as patient discomfort.

As an alternative to time-consuming cryosectioning, unsectioned tissue can be fluorescently labeled, and then optical sectioning can be used to image a single plane from within a bulk specimen. Various methods have been demonstrated for imaging of Mohs and other surgical specimens, including MUSE [6], which uses deep UV illumination to localize fluorescence to the tissue surface, fluorescence confocal microscopy (CFM) [7–10] and nonlinear microscopy (NLM) [11] which use focused laser scanning to excite fluorescence. Early studies using CFM to image Mohs specimens used a single contrast agent, acridine orange (AO) [10,12] and achieved sensitivities approaching 90% as compared to FSA when read by expert readers [7,13]. However, these methods required retraining of the Mohs surgeon to interpret images which had a different appearance than FSA histology. This limitation was addressed by displaying nuclear signals as pseudocolored purple and stromal signals as pseudocolored pink in analogy with hematoxylin and eosin (H&E) histology. This was first implemented using acridine as the nuclear contrast, and backscattered light as the stromal contrast [14], and then improved by introducing eosin yellow (EY) as the stromal contrast [15].

Concurrent with initial CFM studies in skin, NLM of breast tissue using AO and second harmonic generation (SHG) was demonstrated [16] along with more realistic nonlinear absorption models [17] that improve contrast. Subsequently, the use of the red-shifted eosin-related dye sulforhodamine 101 for NLM imaging [18] and ATTO dyes for MUSE [19] enabled concurrent imaging of both the nuclear and stroma channels in breast [20] and prostate [21] more rapidly than was possible using the spectrally overlapped dyes AO and EY. In addition, the use of nonlinear excitation enables substantially deeper imaging into tissue specimens [22] as well as reduced sensitivity to obscuration from surgical debris, blood or tissue marking inks.

Although technical advances in staining, image processing and deeper volumetric imaging enabled by NLM improve image quality, a key step for clinical translation is to demonstrate that that optical sectioning is diagnostically equivalent to FSA. However, these studies are challenging because FSA histology is obtained from cryosectioned tissue, sectioning a plane from within a specimen, while NLM images intact unfrozen tissue. Consequently, the precise location and orientation of the original frozen section plane are typically lost when the specimen is thawed, complicating direct comparison of NLM and FSA histology. In Mohs surgery, this registration error is further complicated by the heterogenous nature of many tumors, resulting in different histological subtypes being present within different layers of the same lesion. Therefore, registration errors may result in different histological findings between NLM images and frozen sections. Similar challenges also occur in developing other intraoperative applications using NLM as an alternative to FSA, including breast and prostate surgery.

We have developed an NLM imaging protocol incorporating AO/SR101 labeling [18] and improved virtual HE rendering [17]. We show that fluorescent labeling with this protocol does not interfere with subsequent paraffin sections or subsequent immunohistochemistry (IHC). To address limitations of previous studies validating against FSA, we introduce a novel method for achieving precise registration between the NLM images and FSA histology where FSA tissue blocks are cryosectioned to produce a thin tissue section for standard FSA histology and an adjacent thick tissue section for NLM imaging. We demonstrate NLM images of Mohs surgical margins that are precisely co-registered with FSA histological sections, enabling the same tissue features to be visualized on both modalities. This will facilitate larger studies which statistically evaluate diagnostic performance of NLM compared with FSA histology in many pathologies where intraoperative consultation is performed.

2. Methods

2.1. Tissue preparation

All tissue selection and imaging were performed using protocols approved by the Massachusetts Institute of Technology Committee on the Use of Humans as Experimental Subjects and Beth Israel Deaconess Medical Center (BIDMC) Committee on Clinical Investigations and Institutional Review Board. Because the tissue sections were taken from residual tissue that was not required for diagnosis, both committees waived the requirement for informed consent. Mohs specimens were obtained from patients undergoing surgery for BCC at BIDMC. Following standard clinical practice, after excision, relaxing incisions were introduced as necessary to flatten each specimen, and optimal cutting temperature (OCT) media was used to support tissue while freezing it under compression against a heat extractor (Fig. 1(a-c)). Following freezing, the tissue block was cryosectioned to produce FSA histology slides for intraoperative evaluation (Fig. 1(d)). Following confirmation that the FSA histology is satisfactory for clinical assessment, the remaining tissue in the frozen block is not used for clinical diagnosis and discarded. An additional thick tissue section (~50 μm) were cryosectioned from the unused frozen tissue block immediately below the final FSA plane using during margin evaluation (Fig. 1(e)) for NLM imaging and comparison. The thick specimen was transferred to a slide and thawed in alcohol before NLM imaging (Fig. 1(f)). Crucially, because the NLM tissue specimen is sectioned from the remaining frozen block prior to thawing, the release of tension on the residual tissue during thawing does not deform the NLM specimen, enabling precise co-registration of NLM images with the FSA section. If the tissue in the block were thawed for NLM imaging, retraction of the tissue during thawing would introduce discordance between the NLM image and FSA histological planes.

Following surgery, the FSA histology slides were scanned using a whole slide scanner (Philips UFS). To test imaging of fresh human tissue which has not been frozen, additional skin was obtained from discarded 'dog-ear' specimens removed during surgery. This is normal tissue that is removed during wound repair but not used for clinical assessment. Following collection, specimens were fluorescently labeled using a protocol described previously [18] for breast tissue that consists of 1 minute immersion in 40 μg/ml acridine orange (AO) combined with 40 μg/ml sulforhodamine 101 (SR101) dissolved in 95% ethanol, followed by 10 seconds rinse in buffered saline. The concentration of alcohol used was increased from 50% used previously, to 95% for this protocol. This avoids a rehydration step since Mohs tissue sections are saved in 95% ethanol in the clinic after thawing. Following rinsing, specimens were mounted under a coverslip for NLM imaging.

2.2. NLM imaging and image processing

NLM imaging was performed using a Ti:Sapphire laser (Mira 900-F, Coherent), a modified commercial nonlinear microscope (Thorlabs, Inc.) with a 20x, 1.0 NA (Olympus XLUMPFL20XW) water immersion objective. AO/SR101 fluorophores are two photon excitable from 700 nm to 1050 nm. In this study 780 nm was used as the excitation wavelength, although longer wavelengths could also be used. Fluorescence was split using a 588 nm, 45 degree dichroic filter, and filtered with 540 ± 20 nm bandpass (AO channel) and 650 ± 30 nm bandpass filters (SR101 channel), then detected using H7422 photomultipliers. One megapixel (1 MP) scans using a 16 kHz resonant galvanometer scanner were performed at 16 Hz frame rate. The imaging area with the 20x objective was 0.49 mm by 0.49 mm. Images were averaged over 10 repeated frames to improve signal to noise (effective frame period of 0.625 ms) followed by a 100 ms time for stage translation. Fields of view were overlapped by 15% to facilitate mosaic generation, for a net acquisition speed of 8.3 minutes per cm^2 of tissue. Vignette correction, per channel gain normalization such that 0.01% of pixels were saturated and VHE rendering [17] were applied
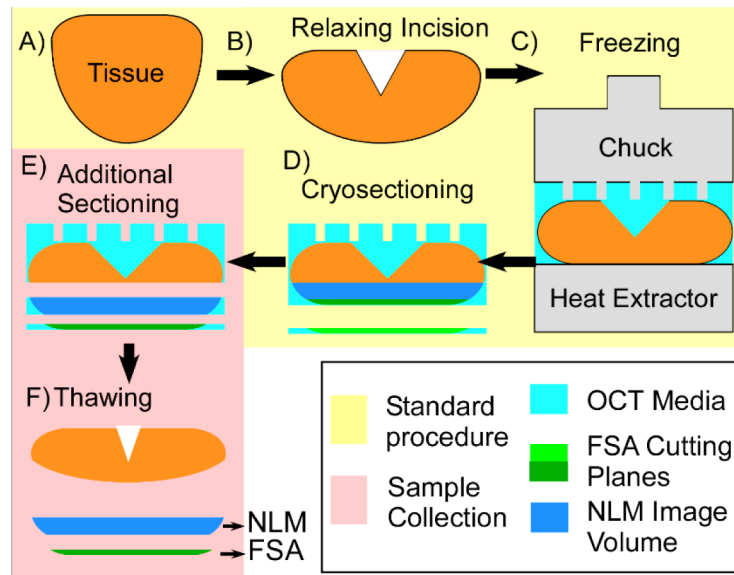
Fig. 1. Method used to NLM image Mohs surgical specimens (red) with precise registration to FSA histology. A) Saucer-shaped tissue specimen is removed during surgery. B) Relaxing incisions are made to partially flatten the tissue. C) The tissue is fully flattened against a heat extractor and frozen in optimal cutting temperature (OCT) media. D) The tissue is cryosectioned to produce an FSA slide for margin evaluation. E) At this stage the block is no longer required for diagnosis and is discarded. An additional FSA section and a thicker volume of frozen tissue are sectioned for study immediately adjacent to the final FSA plane used during margin evaluation. F) Thawing the frozen block distorts the bulk tissue, but there is minimal distortion of the section used for NLM imaging.

to individual frames, which were then stitched into seamless mosaics using Image Composite Editor (Microsoft Research).

3.   Mohs surgical margin imaging

3.1.   Margins negative for basal cell carcinoma

Figure 2 shows an excision margin from the cheek that is negative for BCC using NLM (left) and FSA (right). Using the precise registration enabled by our specimen preparation and imaging protocol, individual features in FSA can be compared directly to NLM images acquired from a plane a few microns away. These include regions of inked subcutaneous fat (green box), visible as a red fluorescent signal on top of delicate, but clearly resolved adipocytes (NLM) and as thin line of red ink on top of a region of tissue destroyed by FSA cryosectioning. Adipose tissue structure is often difficult to preserve in cryosectioning, a limitation which is not present with optically sectioning in NLM. Examination of the superficial skin surface (blue box) shows a well-defined epidermis as well as pilosebaceous units and a small retention cyst in both modalities. The retention cyst (hidrocystoma) contains weakly eosinophilic material which is visible under NLM only. On FSA the cyst contents were likely lost during the frozen sectioning. While the epidermis is well-resolved in both NLM and FSA images, it is noticeably more eosinophilic under NLM. This may reflect intrinsic differences in staining between SR101 and conventional eosin, or differences in how efficiently the highly water-soluble stains are rinsed out of thin frozen sections compared to the much thicker NLM specimens.
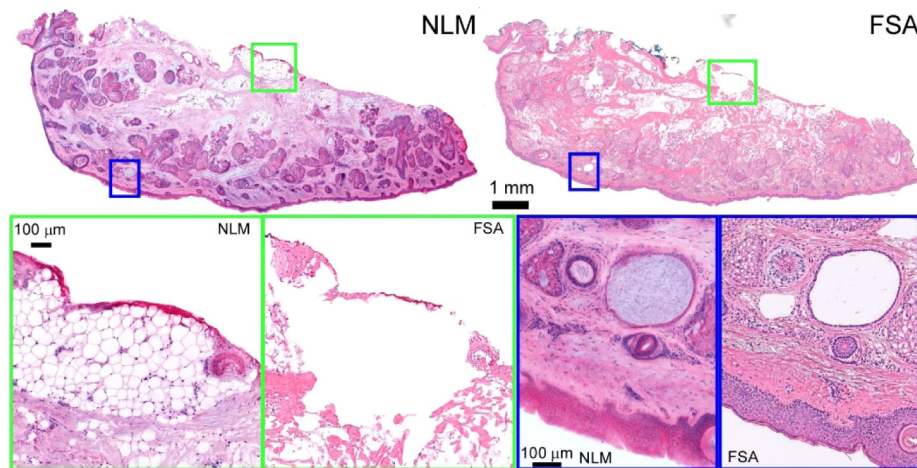
Fig. 2. Normal skin removed during Mohs surgery. High magnification of adipose tissue (green inset), shows adipocytes with red surgical marking ink. Fat is difficult to freeze and appears distorted in FSA histology, while NLM better represents the original tissue appearance. Higher magnification views of the epidermis (blue) show normal structure with sebaceous glands, hair follicles and a hidrocystoma. Full resolution: http://imstore.mit.edu/mohs-boe/Fig2/Fig2.html.

3.2. Margins positive for basal cell and squamous cell carcinoma

Figure 3 shows a Mohs excision margin positive for BCC. The upper half of the specimen has localized areas of nodular BCC as well as small areas with an infiltrative pattern. The lower half contains normal tissue. The tissue along the top edge was inked with red fluorescent surgical ink (red arrows, see full resolution image link) for orientation during surgery, which is visible as a weakly fluorescent red signal in the NLM image. In contrast, conventional green surgical (green arrows) inks use non-fluorescent dyes which do not appear under NLM.

Figure 4 shows a Mohs surgical margin with a large area of nodular BCC in the dermis. The FSA section plane shows the smaller area of BCC because it is closer to the surgical margin. The NLM specimen is sectioned deeper in the specimen and shows a larger area of BCC because it is further from the surgical margin and intercepts more of the tumor. Aside from these differences in sectioning planes, the two images have a high degree of concordance.

Figure 5 shows a Mohs surgical margin with involvement of the subcutaneous tissue by an infiltrative basal cell carcinoma. The specimen was bisected during grossing to facilitate flattening the epidermal tissue edge for cryosectioning. Aside from minor differences in the intensity of SR101 staining of the epidermis as compared to eosin, there is an extremely high degree of correspondence between the NLM and FSA images.

We also investigated other tumors including squamous cell carcinoma (SCC). As with BCC, we observed rapid and consistent labeling of SCC. Figure 6 shows a margin broadly positive for a very well differentiated SCC within a larger (~2 cm) excision specimen. BCC and SCC are the two most common types of keratinocytic carcinoma treated by Mohs surgery, with reported relative ratios ranging from 1:1 to 4:1 BCC:SCC [1].

3.3. Extraction of fluorescent agents by vacuum infiltration processing

It has been shown that fluorescent dyes do not interfere with the appearance of absorptive stains in skin [12], as expected because the dye concentrations used are 100-fold lower than typical absorptive dyes. The effect of fluorescent dyes on immunohistochemistry (IHC) performed on
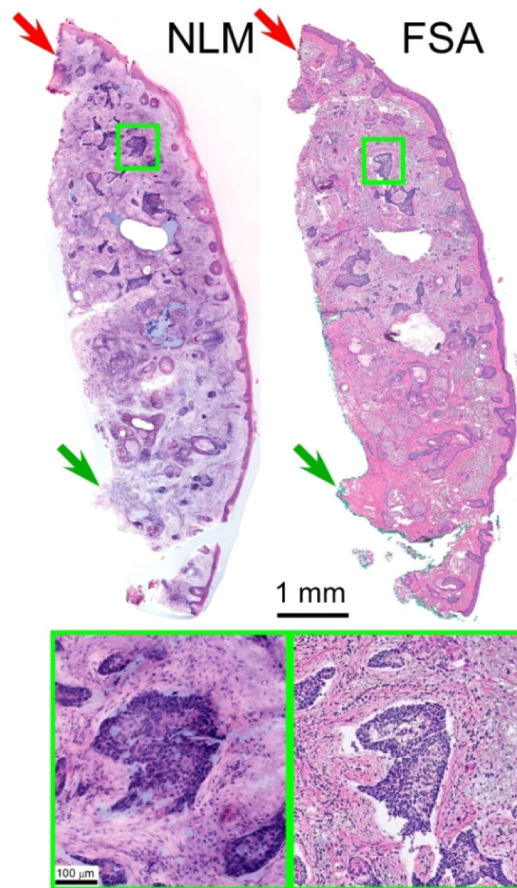
Fig. 3. Mohs margin with mixed nodular and infiltrative pattern BCC. Red surgical marking ink is visible along the top of the figure (red arrows) in both the NLM and FSA images, while green surgical ink (green arrow), which lacks fluorescence, is visible only in the FSA image. Full resolution: http://imstore.mit.edu/mohs-boe/Fig3/Fig3.html.

paraffin sections has been investigated in breast tissue, but not in skin [18]. We hypothesize that because AO and SR101 are highly soluble in xylene, conventional paraffin processing using ethanol dehydration followed by xylene would extract both dyes prior to paraffin embedding, and therefore not interfere with IHC fluorescent labeling. We repeated experiments demonstrated previously in breast [18] where fresh tissue (not previously frozen) was fluorescently labeled for 2 minutes in AO/SR101 (2x longer than required for this protocol), processed on a commercial vacuum infiltration processor until the xylene processing stage, and then removed prior to paraffin infiltration. The xylene cleared tissue was rehydrated and NLM imaged. Two filters sets were used, AO/SR101 fluorescence filters, and second harmonic generation (SHG) filters to detect intrinsic signals from collagen that are not affected by xylene.

Following imaging, the SHG and AO/SR101 NLM images were co-registered using position encoders on the microscope stage (Fig. 7), and the differences in illumination power before and after processing were recorded. Analysis of co-registered pixels containing cell nuclei or SR101 labeled stroma before and after processing showed a > 1000-fold reduction in signal in both AO and SR101 channels, limited by the broad auto-fluorescent background with 780 nm excitation of
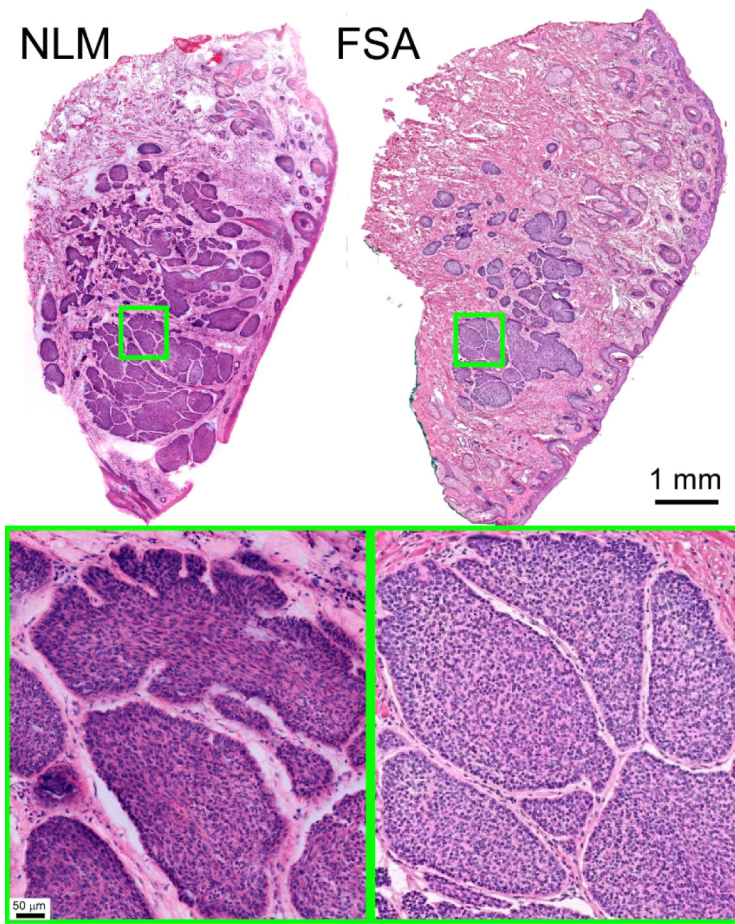
Fig. 4. Excision with large nodular BCC. The FSA section intercepts the edge of the tumor, while the NLM image is from a section tens of microns further into the tumor, showing a larger area of nodular BCC. At low magnification, multiple nodules of basaloid tumor with peripheral palisading form a large deep dermal tumor mass. At higher magnification, palisading of tumor cells at the periphery of the nodule and peritumoral stromal mucin, both characteristics of basal cell carcinomas, are seen equally well on NLM and FSA images. Full resolution: http://imstore.mit.edu/mohs-boe/Fig4/Fig4.html.

skin. Because xylene does not quench either AO or SR101 fluorescence [18], we conclude that both agents were extracted during tissue processing.

Following demonstration that commercial paraffin processing extracts AO/SR101 from fresh human skin, we submitted additional tissue labeled for 2 minutes in AO/SR101 for paraffin processing and then IHC labeling. The concentration of fluorescent dye will decrease with depth into tissue, and paraffin processing can result in the removal of several hundred microns of superficial tissue depending on the tissue alignment with the block face and microtome cutting plane. Therefore, we took superficial sections from the block that corresponded to the precise tissue face where the fluorescent labels concentrations would be highest. We tested two commonly used antibodies in dermatopathology, the melanocytic marker Melan-A and a cytokeratin antibody MNF-116 for epithelial cells (Fig. 8). Neither antibody showed non-specific binding or apparent signal loss after AO/SR101 labeling and subsequent wash-out, consistent with the measurements showing fluorescent agent extraction.
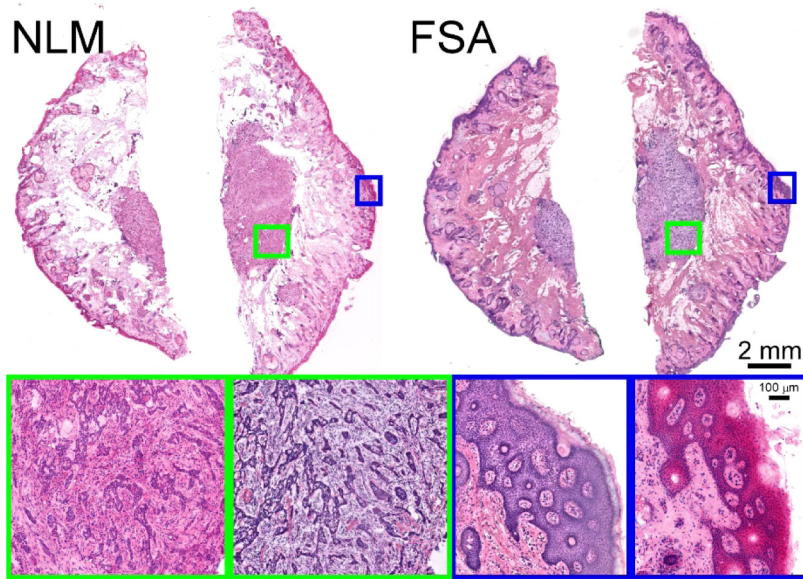
Fig. 5. Mohs excision with a large mass of infiltrative CC. The central portion of each half of the excision contains nests and cords of tumor cells that irregularly infiltrate into the deep fatty subcutaneous tissue. The overlying epidermis is histologically normal. Full resolution: http://imstore.mit.edu/mohs-boe/Fig5/Fig5.html.
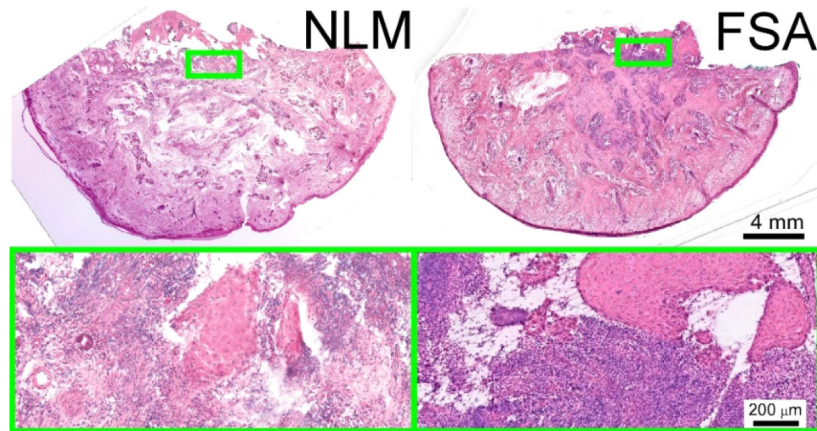

Fig. 6. Mohs excision with well differentiated squamous cell carcinoma (SCC). The high magnification view (bottom) shows a region of invasion. http://imstore.mit.edu/mohs-boe/Fig6/Fig6.html.
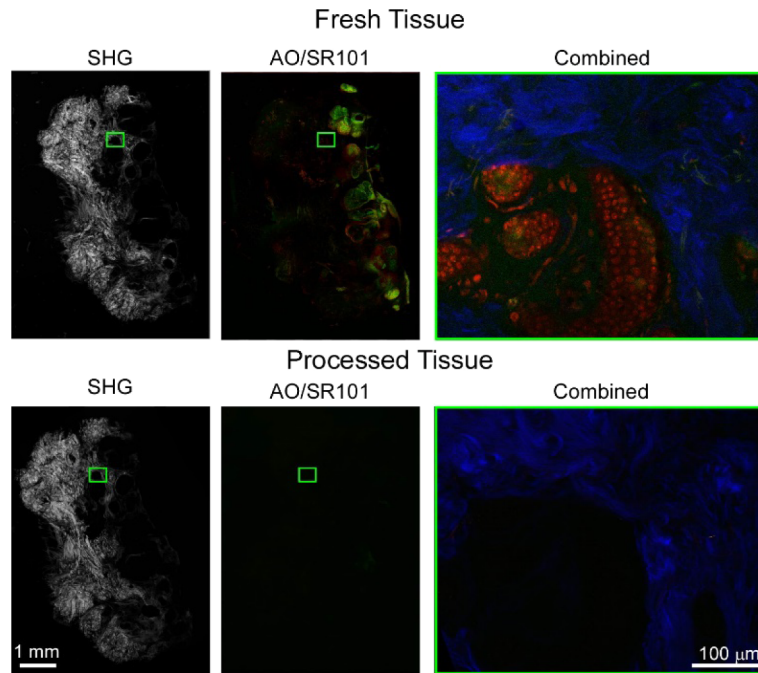
Fig. 7. SHG (left column) and AO/SR101 fluorescence NLM imaging (center column) image of fresh human skin (not frozen) both before (top row) and after (bottom) fixation and processing on a vacuum infiltration processor. SHG is almost completely unaffected by vacuum infiltration processing because it is an intrinsic signal produced by collagen, which is not soluble in either ethanol or xylene. In contrast, the highly soluble AO and SR101 labels are reduced to undetectable levels after processing. In the right column, a magnified view of a sebaceous gland with SHG (blue), AO (red) and SR101 (green) shows the collagen is unchanged after vacuum processing, but the fluorescent signal from cell nuclei is reduced to undetectable levels.
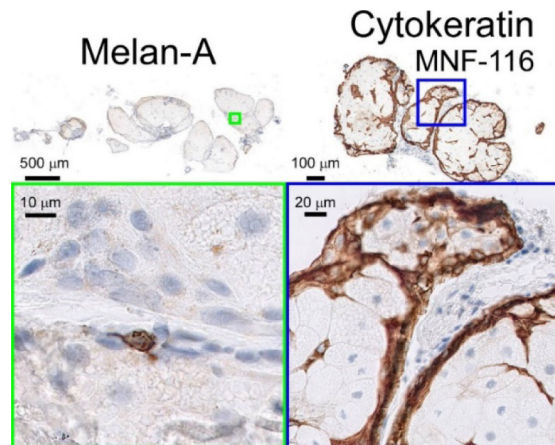

Fig. 8. Demonstration of IHC on tissue after AO/SR101 labelling and washout. Melan-A (left panel) highlights the cytoplasm of an isolated melanocyte within the sebaceous gland, with a high signal and without non-specific labeling of other cell types. Similarly, we observed high signal and specific cytokeratin labeling of the basal layer is a sebaceous lobule (right panel). These results are consistent with the finding that AO/SR101 are extracted from tissue.

4. Discussion

Tissue distortion from histological processing has been a confounding problem for studies investigating the correspondence and diagnostic performance of imaging technologies such as NLM compared with standard methods such as FSA histology. We introduced a protocol that enables precise co-registration of NLM fluorescence images with FSA histology. Because Mohs skin tissue specimens are typically "saucer-shaped" or otherwise curved, normal FSA processing uses relaxing incisions to mechanically flatten specimens by compressing them onto the heat extractor during freezing. However, the specimen relaxes towards its original shape on thawing, distorting the FSA sectioning plane. Our protocol sections and images tissue immediately adjacent to the FSA sectioning plane from the bulk tissue in the frozen block, removing the strain that would otherwise distort the image plane during thawing. We cut 50 μm thick sections (>25 times the NLM axial resolution), enabling 3D NLM imaging of tissue. We used this protocol to image Mohs surgical specimens with NLM and conventional FSA, achieving dramatically better co-registration than previously possible. While this manuscript describes Mohs surgical margins, this protocol is generally applicable to any FSA specimens and will be valuable in future studies to evaluate sensitivity and specificity of NLM compared with FSA histology. This protocol also has the advantage that it does not interfere with clinical diagnosis because it only requires obtaining an additional 50 μm thick section from the tissue block, preserving tissue which may be required for additional histological evaluation.

We further describe a staining protocol for dermatological imaging that incorporates acridine orange (AO), a dye used previously to image Mohs specimens, and sulforhodamine 101 (SR101), a fluorescent label that has similar affinity for tissue as eosin, but that has a red-shifted emission as compared to eosin-Y, enabling the emission spectra to be separated by wavelength [18]. The ability to spectrally separate the stromal (SR101) and nuclei channels (AO) enables rapid evaluation of surgical specimens because it avoids the need to sequentially illuminate each channel. Labeling with AO/SR101 requires only 60 seconds for deep imaging, and only a few seconds for surface imaging, simultaneously labeling both DNA and stroma. Finally, we verified that both frozen and never frozen fresh tissue label with AO/SR101.

We observed that the appearance of nodular, infiltrative and superficial BCC specimens as well as SCC was similar between both FSA and NLM. Normal skin features, including the normal compartments, appendage structures and neurovascular and supporting tissues were all immediately recognizable in NLM images with only minor differences in staining hue as compared to FSA. Some features such as the epidermis were more eosinophilic under SR101 labeling, either due to differences in the intrinsic affinities of SR101 and eosin-Y, or possibly due to differences in how efficiently thin frozen sections can be rinsed as compared to the thicker tissue imaged under NLM. Similarly, smooth muscle was more strongly labeled by SR101 than by eosin-Y. Other features, such as adipocytes were better preserved under NLM imaging than FSA. These results suggest that AO/SR101 labeling and NLM imaging can provide similar contrast to conventional FSA using hematoxylin and eosin.

We verified that AO/SR101 stained tissue can be processed using conventional vacuum infiltration processing to yield paraffin sections where fluorophores are undetectable below the background tissue autofluorescence. We confirmed that these sections stain normally using Melan-A and cytokeratin MNF-116 antibodies, indicating that NLM fluorescent labeling does not interfere with two common cutaneous IHC stains. Crucially, Melan-A highlighted melanocytes on fluorescently labeled tissue with high affinity, indicating that if incidental melanocytic proliferations including melanoma are discovered during Mohs procedures, fluorescent dyes are unlikely to interfere with subsequent IHC characterization.

The NLM imaging speeds of ~8 min/cm^2 used here are sufficient for investigating the sensitivity and specificity of NLM compared with FSA histology, but are insufficient for Mohs clinical workflow. However the main purpose of this study was to demonstrate tissue staining for NLM

and a protocol that enables precise registration of NLM images with FSA histology. The NLM instrument was built using a commercial system and averaged 10 repeated frames with a time consuming stage translation to acquire different fields. Speeds can be dramatically increased if lower magnifications can be used and by redesigning the instrument.

Mohs FSA histology specimens are typically first examined with a wide field at low magnification using a 2x or 4x objective to identify regions of interest, then viewed at higher magnification using a 10x or 20x objective to detect pathology. If high magnification is required for both functions, a high magnification mosaic image of the entire specimen will be needed prior to examination. Mosaic images provide wide field of view and can be rapidly panned and zoomed, but would necessitate instrument redesign to achieve clinically acceptable acquisition times. NLM has a trade-off between field of view and axial section thickness because lower numerical aperture (NA) wide field objectives have thicker sectioning and blur image features. Therefore is important to determine the magnifications and NAs (sectioning thickness) required to detect pathology vs identify suspicious regions.

While the diagnostic features of the most common BCC subtypes are similar in NLM and FSA histology, larger studies are required to establish the sensitivity and specificity for each subtype. In addition, studies of SCC subtypes will also be important because they can account for 20% to 50% of the NMSCs treated by Mohs surgery [1].

5. Conclusion

We demonstrated a staining protocol and NLM imaging on Mohs specimens of BCC and SCC which generates images comparable to FSA histology and does not interfere with IHC. We also present a new protocol for obtaining precise co-registration between NLM images and FSA histology. This capability will be critical for performing studies which evaluate the diagnostic performance of NLM versus FSA histology in the future and will be a key step in the clinical translation of NLM technology. In addition to Mohs surgery, these methods can be applied to a wide range of pathologies where FSA would be used for intraoperative consultation.

Disclosures

The authors declare that there are no conflicts of interest related to this article.

References

1. H. W. Rogers, M. A. Weinstock, S. R. Feldman, and B. M. Coldiron, "Incidence Estimate of Nonmelanoma Skin Cancer (Keratinocyte Carcinomas) in the US Population, 2012," JAMA Dermatol. **151**(10), 1081–1086 (2015).
2. American Cancer Society, "Cancer Facts & Figures 2018," http://www.cancer.org/research/cancerfactsstatistics/cancerfactsfigures2016/.
3. K. V. Viola, M. Jhaveri, P. Soulos, R. Turner, W. Tolpinrud, D. Doshi, and C. P. Gross, "Mohs micrographic surgery and surgical excision for nonmelanoma skin cancer treatment in the Medicare population," Arch. Dermatol. **148**(4), 473–477 (2012).
4. I. Leibovitch, S. C. Huilgol, D. Selva, S. Richards, and R. Paver, "Basal cell carcinoma treated with Mohs surgery in Australia II. Outcome at 5-year follow-up," J. Am. Acad. Dermatol. **53**(3), 452–457 (2005).
5. E. P. Tierney and C. W. Hanke, "Cost effectiveness of Mohs micrographic surgery: review of the literature," J. Drugs Dermatol. **8**(10), 914–922 (2009).

6. T. Yoshitake, M. G. Giacomelli, L. M. Quintana, H. Vardeh, L. C. Cahill, B. E. Faulkner-Jones, J. L. Connolly, D. Do, and J. G. Fujimoto, "Rapid histopathological imaging of skin and breast cancer surgical specimens using immersion microscopy with ultraviolet surface excitation," Sci. Rep. **8**(1), 4476 (2018).

7. C. Longo, M. Rajadhyaksha, M. Ragazzi, K. S. Nehal, S. Gardini, E. Moscarella, A. Lallas, I. Zalaudek, S. Piana, G. Argenziano, and G. Pellacani, "Evaluating ex vivo fluorescence confocal microscopy images of basal cell carcinomas in Mohs excised tissue," Br. J. Dermatol. **171**(3), 561–570 (2014).

8. S. Abeytunge, Y. Li, B. Larson, G. Peterson, E. Seltzer, R. Toledo-Crow, and M. Rajadhyaksha, "Confocal microscopy with strip mosaicing for rapid imaging over large areas of excised tissue," J. Biomed. Opt. **18**(6), 061227 (2013).

9. J. Bini, J. Spain, K. S. Nehal, V. Hazelwood, C. A. DiMarzio, and M. Rajadhyaksha, "Confocal mosaicing microscopy of human skin ex vivo: spectral analysis for digital staining to simulate histology-like appearance," J. Biomed. Opt. **16**(7), 076008 (2011).

10. J. K. Karen, D. S. Gareau, S. W. Dusza, M. Tudisco, M. Rajadhyaksha, and K. S. Nehal, "Detection of basal cell carcinomas in Mohs excisions with fluorescence confocal mosaicing microscopy," Br. J. Dermatol. **160**(6), 1242–1250 (2009).

11. M. Balu, C. B. Zachary, R. M. Harris, T. B. Krasieva, K. König, B. J. Tromberg, and K. M. Kelly, "In Vivo Multiphoton Microscopy of Basal Cell Carcinoma," JAMA Dermatol. **151**(10), 1068 (2015).

12. D. S. Gareau, Y. Li, B. Huang, Z. Eastman, K. S. Nehal, and M. Rajadhyaksha, "Confocal mosaicing microscopy in Mohs skin excisions: feasibility of rapid surgical pathology," J. Biomed. Opt. **13**(5), 054001 (2008).

13. A. Bennàssar, A. Vilata, S. Puig, and J. Malvehy, "Ex vivo fluorescence confocal microscopy for fast evaluation of tumour margins during Mohs surgery," Br. J. Dermatol. **170**(2), 360–365 (2014).

14. D. S. Gareau, "Feasibility of digitally stained multimodal confocal mosaics to simulate histopathology," J. Biomed. Opt. **14**(3), 034050 (2009).

15. D. S. Gareau, A. Bar, N. Snaveley, K. Lee, N. Chen, N. Swanson, E. Simpson, and S. Jacques, "Tri-modal confocal mosaics detect residual invasive squamous cell carcinoma in Mohs surgical excisions," J. Biomed. Opt. **17**(6), 066018 (2012).

16. Y. K. Tao, D. Shen, Y. Sheikine, O. O. Ahsen, H. H. Wang, D. B. Schmolze, N. B. Johnson, J. S. Brooker, A. E. Cable, J. L. Connolly, and J. G. Fujimoto, "Assessment of breast pathologies using nonlinear microscopy," Proc. Natl. Acad. Sci. **111**(43), 15304–15309 (2014).

17. M. G. Giacomelli, L. Husvogt, H. Vardeh, B. E. Faulkner-Jones, J. Hornegger, J. L. Connolly, and J. G. Fujimoto, "Virtual Hematoxylin and Eosin Transillumination Microscopy Using Epi-Fluorescence Imaging," PLoS One **11**(8), e0159337 (2016).

18. L. C. Cahill, M. G. Giacomelli, T. Yoshitake, H. Vardeh, B. E. Faulkner-Jones, J. L. Connolly, C.-K. Sun, and J. G. Fujimoto, "Rapid virtual hematoxylin and eosin histology of breast tissue specimens using a compact fluorescence nonlinear microscope," Lab. Invest. **98**(1), 150–160 (2018).

19. W. Xie, Y. Chen, Y. Wang, L. Wei, C. Yin, A. K. Glaser, M. E. Fauver, E. J. Seibel, S. M. Dintzis, J. C. Vaughan, N. P. Reder, and J. T. C. Liu, "Microscopy with ultraviolet surface excitation for wide-area pathology of breast surgical margins," J. Biomed. Opt. **24**(02), 1–11 (2019).

20. M. G. Giacomelli, T. Yoshitake, L. C. Cahill, H. Vardeh, L. M. Quintana, B. E. Faulkner-Jones, J. Brooker, J. L. Connolly, and J. G. Fujimoto, "Multiscale nonlinear microscopy and widefield white light imaging enables rapid histological imaging of surgical specimen margins," Biomed. Opt. Express **9**(5), 2457–2475 (2018).

21. L. C. Cahill, J. G. Fujimoto, M. G. Giacomelli, T. Yoshitake, Y. Wu, D. I. Lin, H. Ye, O. M. Carrasco-Zevallos, A. A. Wagner, and S. Rosen, "Comparing histologic evaluation of prostate tissue using nonlinear microscopy and paraffin H&E: a pilot study," Mod. Pathol. (2019).

22. T. Yoshitake, M. G. Giacomelli, L. C. Cahill, D. B. Schmolze, H. Vardeh, B. E. Faulkner-Jones, J. L. Connolly, and J. G. Fujimoto, "Direct comparison between confocal and multiphoton microscopy for rapid histopathological evaluation of unfixed human breast tissue," J. Biomed. Opt. **21**(12), 126021 (2016).